PAPER

Check for updates

Efficient plasmonic water splitting by heteroepitaxial junction-induced faceting of gold nanoparticles on an anatase titanium(IV) oxide nanoplate array electrode†

Shin-ichi Naya,[a] Yoko Morita,[b] Hisashi Sugime, [ID][b,c] Tetsuro Soejima, [ID][b,c] Musashi Fujishima[b,c] and Hiroaki Tada [ID] *[d]

Plasmonic photocatalysts represented by gold nanoparticle (NP)-loaded titanium(IV) oxide (Au/TiO$_2$) can be promising solar-to-fuel converters by virtue of their response to visible-to-near infrared light. Hitherto, Au/rutile (R)-TiO$_2$ has been recognized as exhibiting photocatalytic activity higher than that of Au/anatase (A)-TiO$_2$. Herein, we demonstrate that the high potential of A-TiO$_2$ as the Au NP support can be brought out through atomic level interface control. Faceting of Au NPs is induced by a heteroepitaxial junction on an A-TiO$_2$(001) nanoplate array (Au/A-TiO$_2$ NPLA). Photoexcitation towards the Au/A-TiO$_2$ NPLA electrode generates current for the water oxidation reaction at $\lambda < 900$ nm with a maximum efficiency of 0.39% at $\lambda = 600$ nm, which is much larger than the values reported so far for the usual electrodes. The striking activity of the Au/A-TiO$_2$ NPLA electrode was rationalized using a potential-dependent Fowler model. This study presented a novel approach for developing solar-driven electrodes for green and sustainable fuel production.

Introduction

An ultimate goal of science and technology is the construction of artificial photosynthesis systems with water splitting as a benchmark.[1,2] Photoelectrochemical (PEC) water splitting assumes an advantage over the photocatalytic process using particles because of the inhibition of the back reaction and safety due to the spatial separation of the reaction fields where hydrogen (H$_2$) and oxygen (O$_2$) are generated. The key to achieving efficient PEC water splitting is the development of highly active photoanodes for the water oxidation reaction (WOR) with large activation energy.[3] In a typical *n*-TiO$_2$ photoanode, the performance is severely limited by the slow kinetics of the holes with a diffusion length of as small as ~10 nm (ref. 4) and its response only to UV light accounting for ~3% of the solar energy. In view of effective solar energy utilization, plas-

monic photocatalysts represented by gold nanoparticle-loaded TiO$_2$ (Au/TiO$_2$) have recently attracted much interest on account of their wide spectral response from visible to near-infrared light.[5–16] Also, the problem of sluggish hole transport in n-type semiconductor photoanodes can be eliminated in the WOR using the Au/TiO$_2$ plasmonic electrode because water is oxidized by the holes generated in Au NPs *via* localized surface plasmon resonance (LSPR) excitation without requiring their diffusion. While intensive efforts have been devoted to increase the incident photon-to-current efficiency (IPCE) of the Au/TiO$_2$ electrode through several approaches, such as Au–Ag alloying,[17] lithium intercalation into TiO$_2$,[18] and loading promoters for the WOR,[19,20] it is also a great challenge in materials sciences to enhance the performance of the prototype Au/TiO$_2$ electrode itself for underpinning the development toward the practical applications in solar-to-fuel conversion. However, in the usual Au/TiO$_2$ plasmonic electrode systems, the incident photon-to-current efficiency (IPCE) for the WOR remains below ~0.03% (Table S1†).[18,21–23] The IPCE is determined by the product of efficiencies in a series of physical processes including light harvesting, hot electron transfer (HET) from Au NPs to TiO$_2$, charge separation, and the chemical process or WOR.[24] All these processes can be affected by various factors including the size[25] and shape[26] of Au NPs, and the crystal form of TiO$_2$.[27] In particular, the IPCE for the WOR by the Au/TiO$_2$ plasmonic electrode sharply

[a]Environmental Research Laboratory, Kindai University, 3-4-1, Kowakae, Higashi-Osaka, Osaka 577-8502, Japan. E-mail: shinichi.naya@itp.kindai.ac.jp
[b]Graduate School of Science and Engineering, Kindai University, 3-4-1, Kowakae, Higashi-Osaka, Osaka 577-8502, Japan
[c]Department of Applied Chemistry, Faculty of Science and Engineering, Kindai University, 3-4-1, Kowakae, Higashi-Osaka, Osaka 577-8502, Japan
[d]Institutes of Innovation for Future Society, Nagoya University, Furo-cho, Chikusa-ku, Nagoya, Aichi 464-8603, Japan. E-mail: hiroaki.tada@mirai.nagoya-u.ac.jp
†Electronic supplementary information (ESI) available. See DOI: https://doi.org/10.1039/d4nr01013b

increases when the Au particle size (d_{Au}) is smaller than 10 nm.[25] In addition, recent experimental and theoretical studies have indicated that strong electronic coupling between an electron acceptor (TiO_2) and electron donors such as plasmonic metal NPs[28,29] and CdS quantum dots[30] through intimate contact can expedite the photoinduced interfacial electron transfer and extend the response light wavelength. Furthermore, the IPCEs of nanostructured TiO_2 electrodes such as the nanotube array (NTA) and nanowire array (NWA), which are one to two orders magnitude greater than that of the conventional mesoporous (mp)-TiO_2 electrode consisting of TiO_2 nanocrystals,[21–23] point to the importance of effective electron transport to the electron collecting electrode on the order of microns in addition to the charge separation *via* the space charge layer formed by the Schottky junction between Au NPs and TiO_2.[31] Since anatase (A)-TiO_2 possesses electron mobility much larger than rutile (R)-TiO_2,[32] A-TiO_2 films with large surface areas have been favourably used as the photoanodes of dye-sensitized solar cells and perovskite solar cells since their invention.[33,34] Strangely, the IPCE for the WOR of Au/A-TiO_2 photoanodes remains at a level comparable to that of Au/R-TiO_2 photoanodes.[21–23] On the other hand, in nanoparticulate Au/TiO_2 plasmonic photocatalyst systems, Au/R-TiO_2 exhibits much higher photocatalytic activity than Au/A-TiO_2 for various reactions[35–40] including the WOR.[27] Recently, the superiority of Au/R-TiO_2 has been found to originate from the $(111)_{Au}//(110)_{R-TiO_2}$ heteroepitaxial (HEPI) junction-induced faceting of Au NPs facilitating the physical processes in the reaction[41] and the increase in the peripheral distance of Au NPs at the interface with TiO_2 or the catalytically active sites for the WOR.[27] Thus, if faceted Au NPs with $d_{Au} <$ 10 nm can be formed on A-TiO_2 by overcoming the general tendency to be hemispherical to minimize the surface area, the enhancement in the IPCE of the Au/A-TiO_2 plasmonic electrode for the PEC WOR is highly expected.

Here, we show that truncated octahedral (t-Oh) Au NPs with $d_{Au} <$ 10 nm can be formed on the A-TiO_2 nanoplate array (NPLA) electrode with dominant (001) surfaces through a HEPI junction with the $(111)_{Au}//(001)_{A-TiO_2}$ orientation, and this t-Oh-Au/A-TiO_2 NPLA electrode exhibits activity for the PEC WOR that is much higher than that exhibited by hemispherical (HS)-Au/A-TiO_2 NPLA and t-Oh Au/R-TiO_2 NWA ones. Moreover, the reason is discussed on the basis of experimental and theoretical simulation results.

Experimental

Materials

Fluorine-doped tin(IV) oxide film-coated glass (FTO, TEC7) and titanium(IV) fluoride (TiF$_4$) were purchased from Aldrich. Tetrabutyl orthotitanate (Ti(OC$_4$H$_9$)$_4$ > 97.0%), hydrochloric acid (HCl > 98.0%), sodium hydroxide (NaOH > 97.0%), hydrogen tetrachloroaurate(III) tetrahydrate (HAuCl$_4$·4H$_2$O > 99%), urea (CH$_4$N$_2$O > 99.0%), and sodium borohydride (NaBH$_4$ >

92.0%) were purchased from Kanto Chemical Co. All chemicals were used as-received without further purification.

Synthesis of the anatase TiO_2 nanoplate array

The anatase TiO_2 nanoplate array (A-TiO_2 NPLA) was synthesized by following reported procedures with slight modification.[42] TiF$_4$ (124 mg) was dissolved in a solution of Ti(OBu)$_4$ (0.17 mL) in 6 M HCl (10 mL) and stirred at room temperature for 15 min. The solution was poured into a Teflon container (volume 25 mL), and FTO (3 cm × 2 cm, 3 pieces) was immersed in the solution. The Teflon container was sealed in a stainless-steel cylinder and heated at 423 K for 18 h. The resulting sample was washed with 0.1 M aqueous NaOH, distilled water, and acetone, and dried *in vacuo* at room temperature to obtain the A-TiO_2 NPLA.

Synthesis of the rutile TiO_2 nanowire array

According the literature,[43] the rutile TiO_2 nanowire array (A-TiO_2 NWA) was hydrothermally synthesized. A solution of Ti(OBu)$_4$ (0.40 mL) in 6 M HCl (10 mL) was poured into a Teflon container (volume 25 mL), and FTO (3 cm × 2 cm, 3 pieces) was immersed in the solution. The Teflon container was sealed in a stainless-steel cylinder and heated at 423 K for 8 h. The resulting sample was washed with distilled water and acetone, and dried *in vacuo* at room temperature. The sample was calcined at 773 K for 8 h in air to obtain the R-TiO_2 NWA.

Au nanoparticle loading

Au nanoparticles were loaded on a TiO_2 electrode by the modified deposition–precipitation method using urea as the neutralizer.[44] Urea (146 mg) was added to an aqueous solution of HAuCl$_4$ (2.43 mM, 10 mL). The TiO_2 electrode was immersed in the solution and heated at 353 K for 18 h. The resulting sample was washed with distilled water and acetone, and dried *in vacuo* at room temperature to obtain an Au^{3+}-adsorbed TiO_2 electrode. The sample was calcined at 673 K for 1 h in air to obtain the Au/TiO_2 electrode. Also, Au NPs were loaded on the TiO_2 electrode by chemical reduction. The Au^{3+}-adsorbed TiO_2 electrode was immersed in an ethanol solution of NaBH$_4$ (1 mM), and left at room temperature for 5 min. The resulting sample was washed with distilled water and acetone. The chemical reduction procedures were repeated 3 times to completely reduce the adsorbed Au^{3+} ions.

Characterization

Scanning electron microscopy (SEM) images and energy dispersive spectroscopic (EDS) elemental mapping were conducted using a Hitachi SU8230 instrument at an applied voltage of 20 kV. Raman spectra were recorded using a Raman spectrometer (JASCO FP-1000) with a green laser (532 nm) as an excitation source. Transmission electron microscopy (TEM) images were obtained using a JEOL JEM-2100F instrument at an applied voltage of 200 kV. X-ray diffraction (XRD) patterns were recorded at 40 kV and 100 mA using a Rigaku SmartLab X-ray diffractometer. The specific surface area was quantified by means of a Micromeritics automatic surface area and poro-

simetry analyzer (TriStar 3000, Shimadzu) *via* nitrogen adsorption–desorption isotherms at 77 K. The samples were measured after degassing at 423 K for 1 h under vacuum. To quantify the Au loading amount, Au NPs were dissolved in aqua regia, and the concentration was determined by inductively coupled plasma spectroscopy (iCAP7600, Shimadzu). UV-Vis-NIR absorption spectra were obtained by the diffuse reflectance method using a UV-2600 spectrometer (Shimadzu) with an integrating sphere unit (Shimadzu, ISR-2600Plus). As the reference, $BaSO_4$ was used for the reflectance (R_∞). The Kubelka–Munk function $[F(R_\infty) = (1 − R_\infty)^2/2R_\infty]$ was used for expressing the relative absorption coefficient. X-ray photoelectron (XP) spectra were measured using a Kratos Axis Nova X-ray photoelectron spectrometer with applied voltage of 15 kV and current of 10 mA using Al Kα as the X-ray source. For the energy reference, the peak of C1s (284.6 eV) was used.

Photoelectrochemical measurements

PEC measurements were carried out using the standard three-electrode electrochemical cell with the structure of $Au/A-TiO_2$ NPLA/FTO (working electrode) | 0.1 M $NaClO_4$ aqueous solution | Ag/AgCl (reference electrode) | glassy carbon (counter electrode). The active area of the working electrode was 4 cm^2 (2 × 2 cm). The electrolyte solution was deaerated by Ar bubbling for 30 min. The working electrode was illuminated using a solar simulator (PEC-L12, Peccell Tech. Inc.) through an optical filter Y-45 (AM 1.5, 1 sun, $\lambda_{ex} > 430$ nm). The linear sweep voltammetry measurements were performed using a galvanostat/potentiostat (HZ-7000, Hokuto Denko). To evaluate the incident photon-to-current efficiencies (IPCEs), the working electrode on the same cells was irradiated by the monochromatic light of a xenon lamp with a monochromator (full width at half-maximum, 10 nm) (HM-5, JASCO). The IPCEs were calculated using eqn (1):

$$\text{IPCE}[\%] = (J_{ph}(E)N_A hc/IF\lambda) \times 100 \tag{1}$$

where $J_{ph}(E)$ is the photocurrent at an electrode potential of E (+0.8 V *vs.* RHE), N_A is the Avogadro constant, I (W cm^{-2}) is the light intensity, F is the Faraday constant, h is the Planck constant, and c is the speed of light. In this study, the photocurrent was measured at the rest potential in the dark.

Also, the solar-to-current efficiency (SCE) was calculated using eqn (2):

$$\text{SCE}[\%] = \int \text{IPCE}(\lambda) \times I_s(\lambda)d\lambda / \int I_s(\lambda)d\lambda \tag{2}$$

where $I_s(\lambda)$ is the light intensity of the sunlight at the wavelength of λ.

PEC impedance spectroscopy (PECIS)

PECIS measurements were carried out using the same cells under the illumination of simulated sunlight ($\lambda_{ex} > 430$ nm, 1 sun). Nyquist plots were obtained from EIS using a frequency response analyzer (HZA-FRA1, Hokuto Denko) built into the galvanostat/potentiostat. The measurements were carried out

by applying a 10 mV AC sinusoidal signal over the frequency range between 100 mHz and 100 kHz. Charge transfer resistance (R_{ct}) values were estimated by a curve fitting for Nyquist plots assuming an RC-equivalent circuit.

Finite difference time domain (FDTD) simulations

Simulation models consist of an Au hemisphere (HS-Au) and an Au truncated octahedron (t-Oh-Au) loaded on a TiO_2 slab (650 × 650 × 50 nm^3), respectively. Au particle sizes were assessed on the basis of the experimental values obtained from TEM observations. Complex refractive indices taken from the literature were used to reproduce the optical responses of these models. The light scattering behaviour of the models was simulated using a total-field scattered-field (TFSF) source. An *x*-polarized plane wave with wavelength from 300 to 1200 nm (f = 250–1000 THz) was generated to illuminate the top of the Au NPs (the zenith of the HS NP or the top plane of the t-Oh NP) from the *z*-axis direction perpendicular to the TiO_2 slab. *E*-field monitors were placed on the *xy* plane ($z = 0$) and the *xz* plane ($y = 0$) to collect local electric field images. Considering the balance between computational cost and accuracy, mesh refinement and perfectly matched layer (PML) with symmetric and/or anti-symmetric boundary conditions were imposed on the models. All of the FDTD simulations were carried out with an Ansys Lumerical FDTD simulation program package.

Results

TiO_2 films were hydrothermally grown on fluorine-doped tin oxide (FTO) substrates from a hydrochloric acid solution of Ti $(OBu)_4$ in the absence and the presence of TiF_4 at 423 K. X-ray diffraction (XRD) patterns of the samples synthesized without and with TiF_4 exhibited peaks at $2\theta = 36.1°$ and $25.3°$ due to diffraction from the (101) planes of $R-TiO_2$ and $A-TiO_2$, respectively (Fig. 1a). The abnormally strong (101) diffraction peaks of $R-TiO_2$ and $A-TiO_2$ indicate that TiO_2 grows with high orientation with respect to the FTO surface in each sample. FTO has weak Raman signals at 634.3 cm^{-1} and 770.6 cm^{-1} assignable to the A_{1g} and B_{2g} modes, respectively (Fig. 1b).[45] The three signals for the sample synthesized without TiF_4 at 234.6 cm^{-1}, 445.6 cm^{-1}, and 609.6 cm^{-1} are assigned to the $B_{1u} + E_u$, E_g, and A_{1g} modes of $R-TiO_2$, respectively.[46] In the spectrum of the sample synthesized with TiF_4, four signals are observed at 145.8 cm^{-1}, 406.0 cm^{-1}, 513.7 cm^{-1}, and 630.8 cm^{-1} due to the E_g, B_{1g}, A_{1g}, and E_g modes of $A-TiO_2$, respectively.[46] Clearly, the addition of TiF_4 to the reaction solution completely changes the crystal form of TiO_2 from rutile to anatase.

Au NPs were loaded on $A-TiO_2$ by the deposition–precipitation (DP) and chemical reduction (CR) methods. The top view (left) and side view (right) scanning electron microscopy (SEM) images of the samples show that the $A-TiO_2$ NPLA (Fig. 1c and d) and the $R-TiO_2$ nanowire array ($R-TiO_2$ NWA, Fig. 1e and f) are grown vertically or obliquely on the FTO films by the hydrothermal processes with and without TiF_4,

Paper
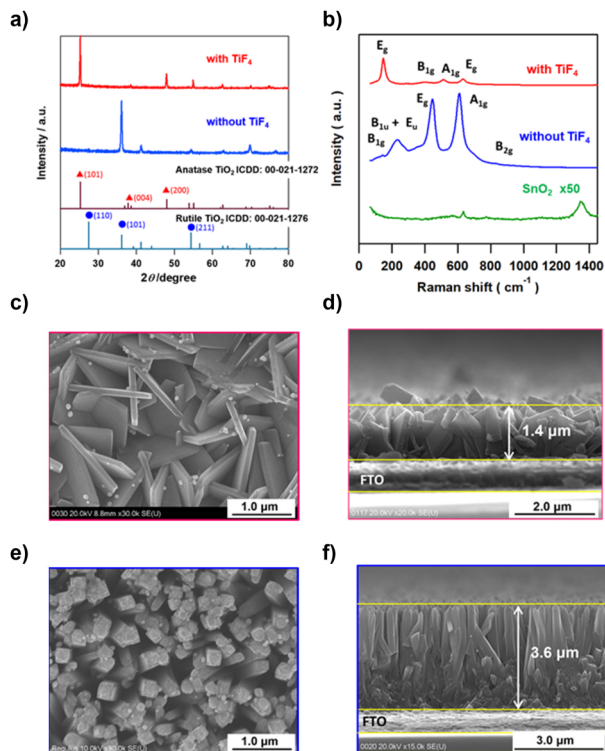
Fig. 1 XRD patterns (a) and Raman spectra (b) of the samples hydrothermally synthesized without and with TiF$_4$. Top view (c) and side view (d) SEM images of the DP-Au/A-TiO$_2$ NPLA. Top view (e) and side view (f) SEM images of the DP-Au/R-TiO$_2$ NWA.

respectively. The A-TiO$_2$ NPLA is composed of NPLs with length ~1.4 μm and thickness ~100 nm, while the dimensions of the R-TiO$_2$ NWs are ~3.6 μm in length and ~200 nm in diameter. In the F$^-$ ion-free system, the Cl$^-$ ions are adsorbed on the R-TiO$_2$(110) surface, and HEPI crystal growth from the FTO substrate occurs in the [001] direction to yield the R-TiO$_2$ NWA.[47] On the other hand, in the F$^-$ ion-added system, TiF$_4$ with a sheet structure can be transformed into an A-TiO$_2$ NPL through hydrolysis.[42] During the growth of A-TiO$_2$ NPLs, the 2D structure is maintained due to the lowering of the surface energy by the preferential adsorption of F$^-$ ions on the (001) facets of the A-TiO$_2$ NPL.[48,49]

In order to study the effects of the Au NP shape, the TiO$_2$ support, and the state of their interface on the activity of the Au/TiO$_2$ plasmonic electrodes for the WOR, the size of Au NPs should be controlled to be approximately equal between samples because the activity is sensitive to NP size. As shown by the transmission electron microscopy (TEM) images, Au NPs are highly dispersed on the A-TiO$_2$ NPLA with d_{Au} of 7.6 ± 1.8 nm by the DP method (Fig. 2a) and 7.9 ± 1.6 nm by the CR method (Fig. S1†). In the high resolution (HR)-TEM image of the DP-Au/A-TiO$_2$ NPL (Fig. 2b), the d-spacings of 1.84 Å and 2.37 Å observed in TiO$_2$ are in agreement with the values of the A-TiO$_2$(200) and (004) crystal planes, respectively. Also, the d-spacings of 2.07 Å and 2.33 Å in the Au NP are close to the values of the Au(100) and (111) crystal planes, respectively.
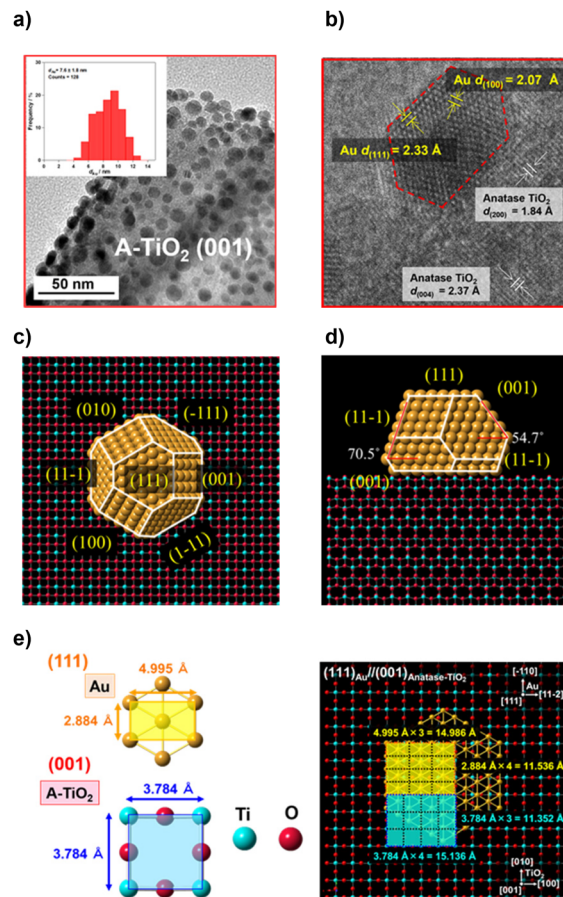
Fig. 2 TEM (a) and HR-TEM (b) images of the DP-Au/A-TiO$_2$ NPLA. Top view (c) and side view (d) of faceted Au NPs on A-TiO$_2$(001) constructed by the Wulff theorem. (e) An interface junction model with the (111)$_{Au}$//(001)$_{A-TiO_2}$ orientation.

Interestingly, faceted Au NPs with a truncated octahedral (t-Oh) shape are formed on A-TiO$_2$ with an atomically commensurate interface between Au(111) and A-TiO$_2$(001). As recently reported for the Au/R-TiO$_2$ NWA,[22] t-Oh Au NPs with d_{Au} = 6.2 ± 1.2 nm are also formed on the (110) side walls of the R-TiO$_2$ NW by the DP method (Fig. S2†). On the other hand, most Au NPs of a CR-Au/A-TiO$_2$ NPL are near-hemispherical (HS) polyhedra (Fig. S1†), and the Au NP-TiO$_2$ interface of the CR-Au/A-TiO$_2$ NPL appears to be of lower quality at an atomic level than the interfaces of the DP-Au/A-TiO$_2$ NPL and DP-Au/R-TiO$_2$ NWA.

The equilibrium shape of Au NPs on the A-TiO$_2$(001) plane was constructed to be a t-Oh by the Wulff theorem using the surface energies of Au(111) (0.72 J m^{-2}), Au(100) (0.87 J m^{-2}), A-TiO$_2$(001) (0.90 J m^{-2}), and the interface energy.[50,51] The interface energy was estimated to be 1.23 J m^{-2} from the contact angle ($\theta \approx 116°$) using the Young equation (Fig. S3†). The top view (Fig. 2c) and side view (Fig. 2d) are very similar to those observed in the TEM image (Fig. 2a) and HR-TEM image (Fig. 2b), respectively. The 2D-rectangular lattices of Au(111) and A-TiO$_2$(001) have the unit dimensions of 4.995 Å × 2.884 Å

and 3.784 Å × 3.784 Å, respectively (Fig. 2e). Fourfold of the d-spacing of Au(−110) crystal planes ($d_{Au(−110)}$) overlaps with threefold of $d_{A-TiO_2(010)}$, and threefold of $d_{Au(11−2)}$ overlaps with fourfold of $d_{A-TiO_2(100)}$ with small mismatches of +1.6% [{(2.884 Å × 4 − 3.784 Å × 3)/3.784 Å × 3} × 100] and −1.0% [{(4.995 Å × 3 − 3.784 Å × 4)/3.784 Å × 4} × 100], respectively, which strongly suggests the formation of the domain-matching epitaxial junction. In the Au/R-TiO$_2$ NW system, a HEPI junction with the orientation of $(111)_{Au}//(110)_{R-TiO_2}$ has been reported to provoke the faceting of Au NPs.[41,52] In a similar manner, the faceting Au NPs can be induced by a domain-matching HEPI junction with the $(111)_{Au}//(001)_{A-TiO_2}$ orientation. The HEPI junction with the same orientation has recently been reported in the system consisting of Au NPs and A-TiO$_2$ nanosheets with dominant (001) surfaces and thickness of ~5 nm.[53]

X-ray photoelectron (XP) spectra of the DP-Au/A-TiO$_2$ NPLA, DP-Au/R-TiO$_2$ NWA, and CR-Au/A-TiO$_2$ NPLA have two signals at binding energies of 83.7 ± 0.1 eV and 87.4 ± 0.1 eV due to emission from the Au4f$_{7/2}$ and 4f$_{5/2}$ orbitals, respectively (Fig. S4†), which are somewhat smaller than the values for the bulk Au (83.9 eV and 87.6 eV).[54] These results indicate that the Au NPs are in a metallic state in every Au/TiO$_2$ system, and the interfacial electron transfer from TiO$_2$ to Au NPs takes place to form the Schottky junction in the dark.[31]

In the Kubelka–Munk-transformed absorption spectra, the A-TiO$_2$ NPLA and R-TiO$_2$ NWA have the absorption edges of 390 nm and 410 nm, which are in agreement with the values for A-TiO$_2$ and R-TiO$_2$, respectively (Fig. 3a).[55] When Au NPs were loaded on TiO$_2$, the absorption due to the LSPR appears in the visible region. The absorption of the DP-Au/A-TiO$_2$ NPLA as well as the DP-Au/R-TiO$_2$ NWA is much stronger and broader than that of the CR-Au/A-TiO$_2$ NPLA. Also, the peak wavelengths (λ_p) of the DP-Au/A-TiO$_2$ NPLA (549 nm) and DP-Au/R-TiO$_2$ NWA (538 nm) are shorter than that of the CR-Au/A-TiO$_2$ NPLA (564 nm). The absorption spectra of CR-Au/A-TiO$_2$ and DP-Au/A-TiO$_2$ NPLAs were calculated for HS and t-Oh Au NPs placed on A-TiO$_2$ employed as their models, respectively, by the finite difference time domain (FDTD) method (Fig. S5†). The spectra indicate that the faceting of Au NPs engenders the enhancement of the LSPR absorption, and the λ_p blueshifts with respect to the value for HS Au NPs. The strong absorption of the DP-Au/R-TiO$_2$ NW with the (110) side walls has recently been attributed to the $(111)_{Au}//(110)_{R-TiO_2}$ HEPI junction-induced faceting of Au NPs.[41] The broadening of the absorption spectrum for the DP-Au/A-TiO$_2$ NPLA is not well reproduced by the simulations. However, the simulated spectrum of t-Oh Au/A-TiO$_2$ possesses several absorption peaks corresponding to different resonance modes (Fig. S6†), while only one resonance peak is observed in the spectrum of the HS-Au/A-TiO$_2$. Thus, the extended LSPR absorption of the DP-Au/A-TiO$_2$ NPLA and DP-Au/R-TiO$_2$ NWA can result from the overlapping of each resonance peak broadened by the polydispersibility of the size and shape of Au NPs, and the significant electronic interaction between Au NPs and TiO$_2$ through the HEPI junction.[40,56]

The current (J)–potential (E) curves of three-electrode PEC cells with the structure of the working electrode | 0.1 M NaClO$_4$ aqueous solution | Ag/AgCl (reference electrode) | glassy carbon (GC, counter electrode) using the DP-Au/A-TiO$_2$ NPLA, CR-Au/A-TiO$_2$ NPLA, and DP-Au/R-TiO$_2$-NWA as the working electrodes were measured (Fig. 3b). The electrode potential (E) is shown with respect to the reversible hydrogen electrode (RHE) below. In each system, current hardly flows in the dark at +0.4 V ≤ E ≤ +1.2 V. The illumination of visible light (AM-1.5, light intensity = 100 mW cm^{-2}, λ > 430 nm) generates anodic current due to the WOR at E > +0.54 ± 0.02 V.[25] Surprisingly, the DP-Au/A-TiO$_2$ NPLA supplies photocurrent far exceeding that of the CR-Au/A-TiO$_2$ NPLA and DP-Au/R-TiO$_2$ NWA, whereas Au/A-TiO$_2$ particles usually show plasmonic photocatalytic activity for the WOR that is much lower than the Au/R-TiO$_2$ ones.[25,41] The specific surface areas of the A-TiO$_2$ NPLA and R-TiO$_2$ NWA were determined to be 5.1 m^2 g^{-1} and 13.6 m^2 g^{-1}, respectively, by the Brunauer–Emmett–Teller (BET) method. The photocurrent normalized by the actual surface area of the DP-Au/A-TiO$_2$ NPLA reaches as much as ~6 times that of the DP-Au/R-TiO$_2$ NWA (Fig. S7†). Clearly, the HEPI junction-induced faceting of Au NPs engenders a drastic increase in the plasmonic WOR activity of Au/A-TiO$_2$ to far surpass even that of the Au/R-TiO$_2$ electrode.
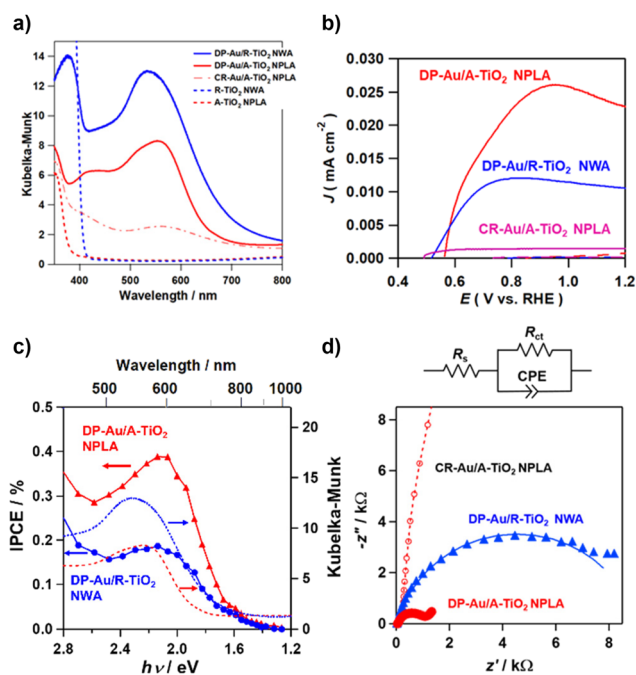
Fig. 3 (a) Kubelka–Munk-transformed absorption spectra of the DP-Au/A-TiO$_2$ NPLA, CR-Au/A-TiO$_2$ NPLA, and DP-Au/R-TiO$_2$ NWA. (b) Current (J)–potential (E) curves in the dark (dotted lines) and under visible light irradiation (λ_{ex} > 430 nm, solid lines). The current density was calculated using the apparent electrode surface area. (c) IPCE action spectra for the WOR with the solar spectrum for comparison (E = 0.8 V vs. RHE). (d) Nyquist plots for the plasmonic electrodes under visible light irradiation (λ_{ex} > 430 nm).

The photocurrents of the DP-Au/A-TiO$_2$ NPLA and DP-Au/R-TiO$_2$ NWA plasmonic electrodes for the WOR were measured under the irradiation of monochromatic light with varying wavelengths (Fig. 3c). The photocurrent flows at λ < 900 nm in each electrode system, and the DP-Au/A-TiO$_2$ NPLA electrode affords IPCEs much greater than those of the DP-Au/R-TiO$_2$ NWA electrode in the whole wavelength region. The maximum IPCE of the former reaches 0.39% at λ = 600 nm, while the value of the latter is 0.18% in accordance with the reported value.[22] Recently, a maximum IPCE of ∼0.06% at λ = 550 nm has been reported for the brookite (B)-TiO$_2$ nanorod array electrode by selectively depositing Au NPs on the lateral {210} surfaces although the interface structure and shape of Au NPs are unclear.[57] Also, each IPCE action spectrum well traces the absorption spectrum, indicating that the photocurrent mainly caused by the 5d–6sp interband excitation of Au NPs[26,58] has to be further enhanced by the LSPR excitation. The redshift in the photocurrent peak of ∼50 nm with respect to the LSPR peak (λ_p) is ascribable to the large dielectric constant of water (80.2 at 293 K)[59] since λ_p is proportional to $(1 + 2\varepsilon_m)^{1/2}$, where ε_m is the dielectric constant of the surroundings.[60] Furthermore, the broad IPCE action spectra of the DP-Au/A-TiO$_2$ NPLA and DP-Au/R-TiO$_2$ NWA electrodes well matches the solar spectrum to afford the solar-to-current efficiency at λ > 430 nm of 0.15% and 0.08%, respectively.

To gain insight into the origin for the high plasmonic photocatalytic activity of the DP-Au/A-TiO$_2$ NPLA for the WOR, PEC impedance analysis was performed for the plasmonic electrodes with an equivalent circuit used for the analysis in which charge transfer resistance (R_{ct}) coupled in parallel with the constant phase element (CFE) is connected in series with ohmic resistance (R_s) (Fig. 3D and Table S2†). In the Nyquist plots under the illumination of visible light (AM-1.5, light intensity = 100 mW cm^{-2}, λ > 430 nm), the R_{ct} corresponding to the diameter of the semicircle decreases in the order of CR-Au/A-TiO$_2$ NPLA (2.4 × 10^5 Ω) ≫ DP-Au/R-TiO$_2$ NWA (9.0 × 10^3 Ω) > DP-Au/A-TiO$_2$ NPLA (1.3 × 10^3 Ω). Evidently, the rate of interfacial charge transfer between the plasmonic electrode and water increases in the order of CR-Au/A-TiO$_2$ NPLA ≪ DP-Au/R-TiO$_2$ NWA < DP-Au/A-TiO$_2$ NPLA.

The local electric field was calculated for HS-Au(d_{Au} = 7.9 nm)/A-TiO$_2$ and t-Oh-Au(d_{Au} = 7.6 nm)/A-TiO$_2$ as the models for the CR-Au/A-TiO$_2$ NPLA and DP-Au/A-TiO$_2$ NPLA, respectively, by the 3D-FDTD method (Fig. 4a and b). In each case, Au NPs were placed on the xy plane of an A-TiO$_2$ slab, and light was irradiated from the z direction perpendicular to the xy plane with the excited localized electromagnetic fields monitored at the xz and xy planes. In the HS-Au/A-TiO$_2$ system, the electric field is uniformly distributed around the periphery of the HS-Au NPs at the interface with A-TiO$_2$ (Fig. 4c). On the other hand, in the t-Oh-Au/A-TiO$_2$ system, an intense electric field is generated around the corners and edges of t-Oh-Au NPs at the interface with A-TiO$_2$ (Fig. 4d and Fig. S6†). The enhancement factor (EF) defined by the square of the ratio of the local electric field intensity to the electric field intensity of incident light was calculated (Table S3†). For
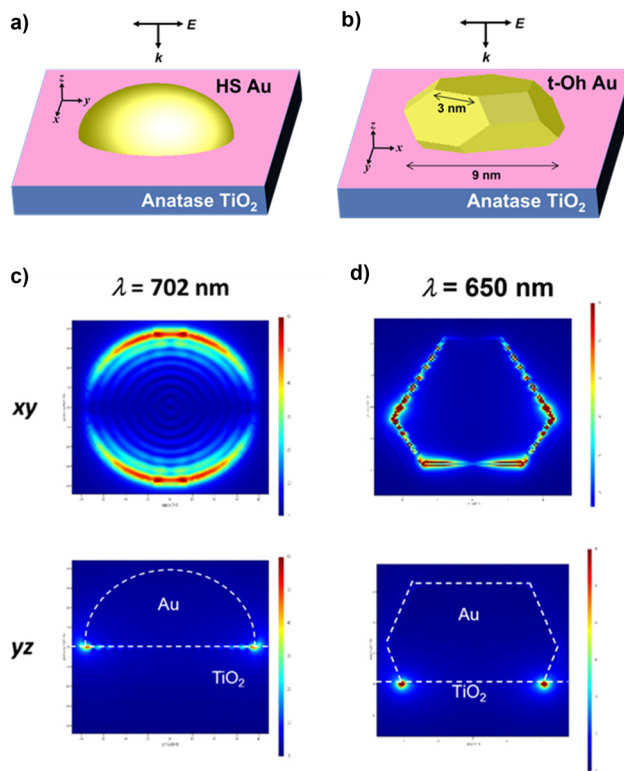

Fig. 4 Local electric fields for HS-Au/A-TiO$_2$ (a) and t-Oh-Au/A-TiO$_2$ (b) calculated by the 3D-FDTD method. Local electric field distributions in HS-Au/A-TiO$_2$ (c) and t-Oh-Au/A-TiO$_2$ (d).

the HS-Au/A-TiO$_2$ system, the maximum EF$_{xz}$ of 2.5 × 10^3 and EF$_{xy}$ of 3.6 × 10^3 are obtained at λ_p = 702 nm. In the t-Oh-Au/A-TiO$_2$ system, the maximum EF$_{xz}$ and EF$_{xy}$ value reaches 1.1 × 10^5 at λ_p = 650 nm, which is greater than the values for the HS-Au/A-TiO$_2$ system by factors of 44 and 31, respectively. The calculations were further performed for t-Oh-Au(d_{Au} = 6.2 nm)/R-TiO$_2$ as the model for the DP-Au/R-TiO$_2$ NWA (Fig. S8a†). An intense electric field localized near the corners and edges at the interface with R-TiO$_2$ is induced by LSPR excitation of the faceted Au NPs (Fig. S8b†). The maximum EF$_{xz}$ and EF$_{xy}$ value of 1.2 × 10^5 at λ_p = 672 nm is comparable to the values of the t-Oh-Au/A-TiO$_2$ system (Table S3†).

Discussion

Truncated octahedral (t-Oh) Au NPs are formed on the large-area (110) side walls of R-TiO$_2$ NWs with high probability by the DP method through the HEPI junction with the (111)$_{Au}$//(110)$_{R-TiO_2}$ orientation.[41] In a similar manner, faceting of Au NPs is induced on A-TiO$_2$ NPLs with dominant (001) surfaces by the (111)$_{Au}$//(001)$_{A-TiO_2}$ HEPI junction during the DP process with a heating temperature of 673 K. A recent *in situ* TEM study has also shown that t-Oh and round-shaped Au NPs are formed on A-TiO$_2$(001) and (101) planes at 773 K, respectively.[61] On the other hand, the room-temperature CR process

produces HS-like Au NPs on A-TiO$_2$ NPLs. Thus, preferential surface exposure of the TiO$_2$ facets that can match the crystal lattice of Au(111) and heating at temperatures above 673 K are necessary for the formation of faceted Au NPs on TiO$_2$ with a high-quality and large-area interface, and long peripheral distance of the Au NPs at the interface with TiO$_2$. The Fermi energy of TiO$_2$ (ε_{F,TiO_2}) can be calculated using the equation of $\varepsilon_{F,TiO_2} = \varepsilon_{CBM} + kT\ln(N_D/N_C)$, where ε_{CBM} is the conduction band (CB) minimum energy of TiO$_2$, k is the Boltzmann constant, N_D is the donor density of TiO$_2$, and N_C is the effective density of states near the CBM of TiO$_2$. The ε_{F,TiO_2} value is estimated to be -5.1 ± 0.1 eV by substituting $\varepsilon_{CBM} = -5.0 \pm 0.1$ eV (ref. 62) and $N_C = 2.5 \times 10^{19}$ cm^{-3} (ref. 63) for the usual N_D value of 10^{17} cm^{-3}. When the Au NP having a large work function ($\Phi_{W,\ Au} = 5.31\text{–}5.47$ eV)[59] comes into direct contact with TiO$_2$ ($\Phi_{W,TiO_2} = 5.1 \pm 0.1$ eV), the interfacial electron transfer proceeds from TiO$_2$ to the Au NP until their Fermi energies are equal. Consequently, a Schottky junction is formed between them at the equilibrium state in the dark.[31]

The IPCE action spectra indicate that the WOR on the Au/TiO$_2$ plasmonic electrode in the present systems is mainly driven *via* the LSPR-induced hot electron transfer (HET) mechanism (Fig. 5).[22,26] When the Au NPs of Au/TiO$_2$ are excited by photons with energy ($\hbar\omega$) larger than the Schottky barrier ($\Delta\varepsilon$), a number of the hot electrons are injected into the CB of TiO$_2$.[25] In the present cases, this energetic requirement is indeed fulfilled because the photocurrent flows at $\hbar\omega > 1.38$ eV (Fig. 3c), which is sufficiently larger than the $\Delta\varepsilon$ of ~0.5 eV reported for the Au/TiO$_2$ system.[31] The electrons injected into the CB of TiO$_2$ can be pulled away from the interface to be transported to the FTO electrode, and the holes are accumulated at the interface according to the potential gradient in the space charge layer. As a result of charge separation, the holes effectively oxidize water at the Au NP-TiO$_2$-liquid triphase interface.[26]

The photocurrent observed for the WOR (J_{ph}) is proportional to the efficiencies of a series of physical processes involving light harvesting (LHE), hot-electron injection (ϕ_{HEI}), and charge separation/transport (ϕ_{CS-CT}) (eqn (3)).[41]
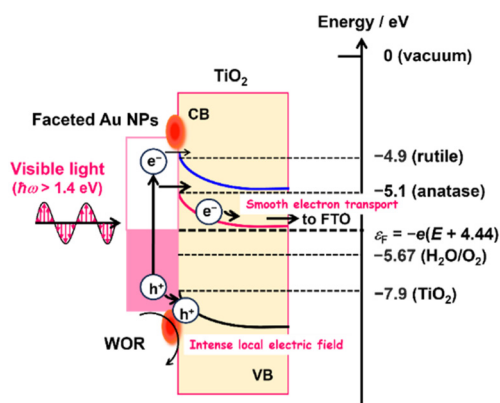

Fig. 5 Action mechanism of the DP-Au/A-TiO$_2$ NPLA and DP-Au/R-TiO$_2$ NWA plasmonic electrodes for the WOR.

Furthermore, the ϕ_{HEI} can be approximated using the Fowler theory (eqn (4)):[31]

$$J_{ph} \propto \text{LHE} \times \phi_{HEI} \times \phi_{CS-CT}. \tag{3}$$

$$\phi_{HEI}(E) \approx C(\hbar\omega - \Delta\varepsilon)^2 / \hbar\omega \tag{4}$$

where E is the electrode potential, C is the constant, and $\Delta\varepsilon$ is the energy difference between the Fermi energy of the Au NP (ε_F) and the ε_{CBM} of TiO$_2$.

As indicated by the absorption spectra (Fig. 3a), the DP-Au/A-TiO$_2$ NPLA and DP-Au/R-TiO$_2$ NWA have LHEs significantly larger than that of the CR-Au/A-TiO$_2$ NPLA, which are induced by the HEPI junctions in the former systems.[24] Also, the ϕ_{HEI} in the LSPR-induced HET mechanism is proportional to the square of the absolute value of the electric field, that is, the EF.[24,64] The EF values of the DP-Au/A-TiO$_2$ NPLA and DP-Au/R-TiO$_2$ NWA are several tens of times larger than that of the CR-Au/A-TiO$_2$ NPLA. Furthermore, the high quality of the Au NP-TiO$_2$ interface in the DP-Au/A-TiO$_2$ NPLA and DP-Au/R-TiO$_2$ NWA contributes to the increase in the ϕ_{HEI}.[65] Therefore, the photocurrents of the DP-Au/A-TiO$_2$ NPLA and DP-Au/R-TiO$_2$ NWA electrodes far surpass that of the CR-Au/A-TiO$_2$ NPLA electrode and are ascribable to the high LHE and extraordinarily large EF values in addition to the higher quality of the interface. However, the large difference in the photocurrent between the DP-Au/A-TiO$_2$ NPLA and DP-Au/R-TiO$_2$ NWA electrodes cannot be explained only in terms of these factors.

Previously, the electron affinity was determined to be 4.9 eV for R-TiO$_2$ and 5.1 eV for A-TiO$_2$ by means of photoemission electron microscopy.[62] Thus, the energy barrier for the HET from Au NPs to TiO$_2$ in the DP-Au/A-TiO$_2$ NPLA electrode is ~0.2 eV lower than that in the DP-Au/R-TiO$_2$ NWA electrode regardless of the electrode potential (Fig. 5). In addition, A-TiO$_2$ possesses an electron mobility of 4–20 cm^2 V^{-1} s^{-1} at 300 K, which is much larger than that for R-TiO$_2$ (0.1 cm^2 V^{-1} s^{-1} at 300 K).[32] In the DP-Au/A-TiO$_2$ NPLA electrode, the electrons injected into the CB of TiO$_2$ can be smoothly separated from the Au NPs and transported to the electron-collecting FTO electrode due to the large electron mobility of A-TiO$_2$.[32] As a result, the hot holes accumulated in the Au NPs are effectively concentrated around the Au NP–TiO$_2$–solution triphase interface to be used for the WOR with the assistance of the catalytic activity,[25,66] which leads to a drastic enhancement of the photocurrent through lowering the R_{ct}. Consequently, the plasmonic activity of the DP-Au/A-TiO$_2$ NPLA, which is much superior to that of the DP-Au/R-TiO$_2$ NWA electrode, can stem from its higher HET efficiency and electric conductivity.

Furthermore, it is worth noting in the electrode system that $\Delta\varepsilon$ in eqn (2) is a function of the electrode potential (E *vs.* standard hydrogen electrode, SHE) or the Fermi energy of the electrode ($\varepsilon_F = -e(E + 4.44)$ *vs.* under vacuum). As a result of the increase in E, the $\Delta\varepsilon$ increases, while the charge separation is enhanced due to the increase in potential gradient and width of the space charge layer. These considerations predict the presence of the optimum potential in the Au/TiO$_2$ plasmonic electrode. Actually, the maximum photocurrents are observed

in the J–E curves at 0.83 V in the DP-Au/R-TiO$_2$ NWA electrode and 0.96 V in the DP-Au/A-TiO$_2$ NPLA electrode (Fig. 3b).

In a particulate photocatalytic system, Chen and Tan have recently reported that a nanohybrid plasmonic photocatalyst consisting of Pt cuboctahedra and radial WO$_3$ mesocrystals provides an apparent quantum efficiency greater than 7% at λ_{ex} = 680 nm for the overall water splitting, which is much larger than that of spherical Pt NP-loaded WO$_3$.[67] This remarkable activity can also arise from the LSPR-induced strong local electric field around the interface between the faceted Pt NPs and WO$_3$. Also, this study points to the importance of the high catalytic activities of Pt NPs for the hydrogen evolution reaction and the oxygen evolution reaction. In this case, it should be noted that both of these catalytic activities can only work simultaneously through the separation of the functions of the Pt NPs as oxidation and reduction sites due to the large absorption of the Pt cuboctahedra and the hierarchical structure of WO$_3$.[68]

In summary, this study aims at enhancing the activity of the prototype plasmonic electrode of Au/TiO$_2$ for the PEC WOR without changing the composition of each component or surface modification by promoters. The t-Oh Au NPs with d_{Au} < 10 nm are formed on the A-TiO$_2$ NPLA with dominant (001) surfaces through the (111)$_{Au}$//(001)$_{A\text{-}TiO_2}$ HEPI junction by the DP process. The resulting DP-Au/A-TiO$_2$ NPLA possesses features including the faceting of the Au NPs and a high-quality interface. The DP-Au/A-TiO$_2$ NPLA electrode has been found to provide an IPCE of 0.39% at λ = 600 nm for the PEC WOR, which is greater than the values reported so far for the usual Au/TiO$_2$ electrodes by more than one order of magnitude. The remarkable activity of the DP-Au/A-TiO$_2$ NPLA plasmonic electrode is ascribable to the intense local electric field generated around the edges and corners of the faceted Au NPs, the high-quality interface between Au NPs and TiO$_2$, and the large electron mobility in A-TiO$_2$, which enhance the physical and chemical processes in the plasmonic WOR. Furthermore, we shed light on the origin of the large difference in the plasmonic activity for the WOR between the DP-Au/A-TiO$_2$ NPLA and DP-Au/R-TiO$_2$ NWA, and the unique features in the photo-current–potential curves in terms of a potential-dependent Fowler model. This marked progress in the performance of the prototype Au/TiO$_2$ plasmonic electrode could contribute to its practical use for solar-to-fuel energy conversion.

Author contributions

S. N., Y. M., H. S. and T. S. prepared and characterized the electrodes, and carried out PEC experiments and data analysis; M. F. performed MD and FDTD calculations; and H. T. supervised the experimental work and data analysis.

Conflicts of interest

There are no conflicts to declare.

Acknowledgements

References

1 A. Fujishima and K. Honda, Electrochemical photolysis of water at a semiconductor electrode, *Nature*, 1972, **238**, 37–38.

2 T. Hisatomi and K. Domen, Reaction systems for solar hydrogen production via water splitting with particulate semiconductor photocatalysts, *Nat. Catal.*, 2019, **2**, 387–399.

3 M. W. Kanan and D. G. Nocera, In situ formation of an oxygen-evolving catalyst in natural water containing phosphate and Co^{2+}, *Science*, 2008, **321**, 1072–1075.

4 L. Zhang, L. Sun, Z. Guan, S. Lee, Y. Li, H. D. Deng, Y. Li, N. L. Ahlborg, M. Boloor, N. A. Melosh and W. C. Chueh, Quantifying and elucidating thermally enhanced minority carrier diffusion length using radius-controlled rutile nanowires, *Nano Lett.*, 2017, **17**, 5264–5272.

5 M. Xiao, R. Jiang, F. Wang, C. Fang, J. Wang and J. C. Yu, Plasmon-enhanced chemical reactions, *J. Mater. Chem. A*, 2013, **1**, 5790–5805.

6 K. Ueno and H. Misawa, Surface plasmon-enhanced photochemical reactions, *J. Photochem. Photobiol., C*, 2013, **15**, 31–52.

7 X. Lang, X. Chen and J. Zhao, Heterogeneous visible light photocatalysis for selective organic transformations, *Chem. Soc. Rev.*, 2014, **43**, 473–486.

8 C. Wang and D. Astruc, Nanogold plasmonic photocatalysis for organic synthesis and clean energy conversion, *Chem. Soc. Rev.*, 2014, **43**, 7188–7216.

9 R. Jiang, B. Li, C. Fang and J. Wang, Metal/semiconductor hybrid nanostructures for plasmon-enhanced applications, *Adv. Mater.*, 2014, **26**, 5274–5309.

10 H. Cheng, K. Fuku, Y. Kuwahara, K. Mori and H. Yamashita, Harnessing single-active plasmonic nanostructures for enhanced photocatalysis under visible light, *J. Mater. Chem. A*, 2015, **3**, 5244–5258.

11 X. Li, J. Zhu and B. Wei, Hybrid nanostructures of metal/two-dimensional nanomaterials for plasmon-enhanced applications, *Chem. Soc. Rev.*, 2016, **45**, 3145–3187.

12 Y. Zhang, S. He, W. Guo, Y. He, J. Huang, J. R. Mulcahy and W. D. Wei, Surface-plasmon-driven hot electron photochemistry, *Chem. Rev.*, 2018, **118**, 2927–2954.

13 N. Wu, Plasmonic metal–semiconductor photocatalysts and photoelectrochemical cells: a review, *Nanoscale*, 2018, **10**, 2679–2696.

14 A. Gelle, T. Jin, L. de la Garza, G. D. Price and L. V. Besteiro, Applications of plasmon-enhanced nanocatalysis to organic transformations, *Chem. Rev.*, 2020, **120**, 986–1041.

15 S. Luo, X. Ren, H. Lin, H. Song and J. Ye, Plasmonic photothermal catalysis for solar-to-fuelconversion: current status and prospects, *Chem. Sci.*, 2021, **12**, 5701–5719.

16 M. Sayed, J. Yu, G. Liu and M. Jaroniec, Non-noble plasmonic metal-based photocatalysts, *Chem. Rev.*, 2022, **122**, 10484–10537.

17 R. S. Haider, S. Wang, Y. Gao, A. S. Malik, N. Ta, H. Li, B. Zeng, M. Dupuis, F. Fan and C. Li, Boosting photocatalytic water oxidation by surface plasmon resonance of Ag_xAu_{1-x} alloy nanoparticles, *Nano Energy*, 2021, **87**, 106189.

18 H. Li, S. Wang, M. Wang, Y. Gao, J. Tang, S. Zhao, H. Chi, P. Zhang, J. Qu, F. Fan and C. Li, Enhancement of Plasmon-Induced Photoelectrocatalytic Water Oxidation over Au/TiO_2 with Lithium Intercalation, *Angew. Chem., Int. Ed.*, 2022, **61**, e202204272.

19 R. Negishi, S. Naya, H. Kobayashi and H. Tada, Gold(core)-lead(shell) nanoparticle-loaded titanium(IV) oxide prepared by underpotential photodeposition: Plasmonic water oxidation, *Angew. Chem., Int. Ed.*, 2017, **56**, 10347–10351.

20 M. Okazaki, Y. Suganami, N. Hirayama, H. Nakata, T. Oshikiri, T. Yokoi, H. Misawa and K. Maeda, Site-selective deposition of a cobalt cocatalyst onto a plasmonic Au/TiO_2 photoanode for improved water oxidation, *ACS Appl. Energy Mater.*, 2020, **3**, 5142–5146.

21 P. A. DeSario, J. J. Pietron, D. E. DeVantier, T. H. Brintlinger, R. M. Stroud and D. R. Rolison, Plasmonic enhancement of visible-light water splitting with Au–TiO_2 composite aerogels, *Nanoscale*, 2013, **5**, 8079–8083.

22 T. Onishi, M. Teranishi, S. Naya, M. Fujishima and H. Tada, Electrocatalytic effect on the photon–to–current conversion efficiency of gold–nanoparticle–loaded titanium(IV) oxide plasmonic electrode for water oxidation, *J. Phys. Chem. C*, 2020, **124**, 6103–6109.

23 S.-F. Hung, F.-X. Xiao, Y.-Y. Hsu, N.-T. Suen, H.-B. Yang, H. M. Chen and B. Liu, Iridium oxide-assisted plasmon-induced hot carriers: Improvement on kinetics and thermodynamics of hot carriers, *Adv. Energy Mater.*, 2016, **6**, 1501339.

24 H. Tada, Rational design for gold nanoparticle–based plasmonic catalysts and electrodes for water oxidation towards the artificial photosynthesis, *Dalton Trans.*, 2022, **51**, 3383–3393.

25 M. Teranishi, M. Wada, S. Naya and H. Tada, Size-dependence of the activity of gold nanoparticle-loaded titanium(IV) oxide plasmonic photocatalyst for water oxidation, *ChemPhysChem*, 2016, **17**, 2813–2817.

26 Y. Nishijima, K. Ueno, Y. Kotake, K. Murakoshi, H. Inoue and H. Misawa, Near-infrared plasmon-assisted water oxidation, *J. Phys. Chem. Lett.*, 2012, **3**, 148–1252.

27 S. Wang, Y. Gao, S. Miao, T. Liu, L. Mu, R. Li, F. Fan and C. Li, Positioning the water oxidation reaction sites in plasmonic photocatalysts, *J. Am. Chem. Soc.*, 2017, **139**, 11771–11778.

28 K. Wu, J. Chen, J. R. McBride and T. Lian, Efficient hot-electron transfer by a plasmon-induced interfacial charge-transfer transition, *Science*, 2015, **349**, 632–635.

29 J. Ma and S. Gao, Plasmon-induced electron-hole separation at the Ag/TiO_2(110) interface, *ACS Nano*, 2019, **13**, 13658–13667.

30 M. Yoshii, H. Kobayashi and H. Tada, Sub-bandgap excitation-induced electron injection from CdSe quantum dots to TiO_2 in a directly coupled system, *ChemPhysChem*, 2015, **16**, 1846–1851.

31 M. W. Knight, H. Sobhami, P. Nordlander and M. J. Halas, Photodetection with active optical antennas, *Science*, 2011, **332**, 702–704.

32 M. Voïnov and J. Augustynski, *Heterogeneous Photocatalysis*, ed. M. Schiavello, John Wiley & Sons, Baffins Lane, 1997.

33 B. O'Regan and M. Grätzel, A low-cost, high-efficiency solar cell based on dye-sensitized colloidal TiO_2 films, *Nature*, 1991, **353**, 737–740.

34 M. M. Lee, J. Teuscher, T. Miyasaka, T. N. Murakami and H. J. Snaith, Efficient hybrid solar cells based on meso-superstructured organometal halide perovskites, *Science*, 2012, **338**, 643–647.

35 E. Kowalska, R. Abe and B. Ohtani, Visible light-induced photocatalytic reaction of gold-modified titanium(IV) oxide particles: action spectrum analysis, *Chem. Commun.*, 2009, **45**, 241–243.

36 E. Kowalska, O. O. P. Mahaney and B. Ohtani, Visible-light-induced photocatalysis through surface plasmon excitation of gold on titania surfaces, *Phys. Chem. Chem. Phys.*, 2010, **12**, 2344–2355.

37 K. Kimura, S. Naya, Y. Jin-nouchi and H. Tada, TiO_2 crystal form-dependence of the Au/TiO_2 plasmon photocatalyst's activity, *J. Phys. Chem. C*, 2012, **116**, 7111–7117.

38 S. Naya, K. Kimura and H. Tada, One-step selective aerobic oxidation of amines to imines by gold nanoparticle-loaded rutile titanium(IV) oxide plasmon photocatalyst, *ACS Catal.*, 2013, **3**, 10–13.

39 J. B. Priebe, J. Radnik, A. J. J. Lennox, M.-M. Pohl, M. Karnahl, D. Hollmann, K. Grabow, U. Bentrup, H. Junge, M. Beller and A. Bruckner, Solar hydrogen production by plasmonic Au-TiO_2 catalsyt: impact of synthesis protocol and TiO_2 phase on charge transfer efficiency and H_2 evolution rates, *ACS Catal.*, 2015, **5**, 2137–2148.

40 S. Naya, T. Niwa, T. Kume and H. Tada, Visible-light-induced electron transport from small to large nanoparticles in bimodal gold nanoparticle-loaded titanium(IV) oxide, *Angew. Chem., Int. Ed.*, 2014, **53**, 7305–7309.

41 S. Naya, A. Akita, Y. Morita, M. Fujishima and H. Tada, Crystallographic interface control of the plasmonic photocatalyst consisting of gold nanoparticles and titanium(IV) oxide, *Chem. Sci.*, 2022, **13**, 12340–12347.

42 S. Feng, J. Yang, H. Zhu, M. Liu, J. Zhang, J. Wu and J. Wan, Synthesis of single crystalline anatase TiO_2 (001)

tetragonal nanosheet-array films fluorine-doped tin oxide substrate, *J. Am. Ceram. Soc.*, 2011, **94**, 310–315.

43 B. Liu and E. S. Aydil, Growth of oriented single-crystalline rutile TiO₂ nanorods on transparent conducting substrates for dye-sensitized solar cells, *J. Am. Chem. Soc.*, 2009, **131**, 3985–3990.

44 R. Zenella, S. Giorgio, C. R. Henry and C. Louis, Alternative methods for the preparation of gold nanoparticles supported on TiO₂, *J. Phys. Chem. B*, 2002, **106**, 7634–7642.

45 A. Dieguez, A. Romano-Rodriguez, A. Vila and J. R. Morante, The complete Raman spectrum of nanometric SnO₂ particles, *J. Appl. Phys.*, 2001, **90**, 1550–1557.

46 O. Frank, M. Zukalova, B. Laskova, J. Kürti, J. Koltai and L. Kavan, Raman spectra of titanium dioxide (anatase, rutile) with identified oxygen isotopes (16, 17, 18), *Phys. Chem. Chem. Phys.*, 2012, **14**, 14567–14572.

47 A. Akita, H. Kobayashi and H. Tada, Action of chloride ions as a habit modifier in the hydrothermal crystal growth of rutile TiO₂ nanorod from SnO₂ seed crystal, *Chem. Phys. Lett.*, 2020, **761**, 138003.

48 H. G. Yang, C. H. Sun, S. Z. Qiao, J. Zou, G. Liu, S. C. Smith, H. M. Chen and G. Q. Liu, Anatase TiO₂ single crystals with a large percentage of reactive facets, *Nature*, 2008, **453**, 638–641.

49 S. Liu, J. Yu and M. Jaroniec, Tunable photocatalytic selectivity of hollow TiO₂ microspheres composed of anatase polyhedra with exposed {001} facets, *J. Am. Chem. Soc.*, 2010, **132**, 11914–11916.

50 D. Holec, P. Dumitraschkewitz, D. Vollath and F. D. Fischer, Surface energy of Au nanoparticles depending on their size and shape, *Nanomaterials*, 2020, **10**, 484.

51 G. Liu, H. G. Yang, J. Pan, Y. Q. Yang, G. Q. Lu and H.-M. Cheng, Titanium dioxide crystals with tailored facets, *Chem. Rev.*, 2014, **114**, 9559–9612.

52 F. Cosandey, L. Zhang and T. E. Madey, Effect of substrate temperature on the epitaxial growth of Au on TiO₂(110), *Surf. Sci.*, 2001, **474**, 1–13.

53 W. Yuan, B. Zhu, K. Fang, X.-Y. Li, T. W. Hansen, Y. Ou, H. Yang, J. B. Wagner, Y. Gao, Y. Wang and Z. Zhang, In situ manipulation of the active Au-TiO₂ interface with atomic precision during CO oxidation, *Science*, 2021, **371**, 517–521.

54 K. Tanaka, S. Tanuma, K. Dohmae, Y. Nagoshi and A. Nisawa, *X-ray photoelectron spectroscopy*, ed. T. Sawada, S. Tanuma and K. Tanaka, Maruzen, Tokyo, 1998.

55 H. Kisch, *Semiconductor Photocatalysis-Principles and Applications* Wiley-VCH, Weinheim, 2015.

56 H. Hovel, S. Fritz, A. Hilger and V. Kreibig, Width of cluster plasmon resonances: Bulk dielectric functions and chemi-cal interface damping, *Phys. Rev. B: Condens. Matter Mater. Phys.*, 1993, **48**, 18178–18188.

57 A. Naldoni, T. Montini, F. Malara, M. M. Mroz, A. Beltram, T. Virgili, C. L. Boldrini, M. Marelli, I. Romero-Ocana, J. J. Delgado, V. Dal Santo and P. Fornasiero, Hot electron collection on brookite nanorods lateral facets for plasmon-enhanced water oxidation, *ACS Catal.*, 2017, **7**, 1270–1278.

58 L. Liu, P. Li, B. Adisak, S. Ouyang, N. Umezawa, J. Ye, R. Kodiyath, T. Tanabe, G. V. Ramesh, S. Ueda and H. Abe, Gold photosensitized SrTiO₃ for visible-light water oxidation induced by Au interband transitions, *J. Mater. Chem. A*, 2014, **2**, 9875–9882.

59 *Handbook of Chemistry and Physics*, ed. D. R. Lide, CRC Press, Boca Raton, 83rd edn, 2002.

60 U. Kreibig and M. Vollmer, *Optical properties of metal clusters*, Springer, Berlin, 1996.

61 W. Yuan, D. Zhang, Y. Ou, K. Fang, B. Zhu, H. Yang, T. W. Hansen, J. B. Wagner, Z. Zhang, Y. Gao and Y. Wang, Direct in situ TEM visualization and insight into the facet-dependent sintering behaviours of gold on TiO₂, *Angew. Chem., Int. Ed.*, 2018, **57**, 16827–16831.

62 G. Xiong, R. Shao, T. C. Droubay, A. G. Joly, K. M. Beck, S. A. Chambers and W. P. Hess, Photoemission electron microscopy of TiO₂ anatase films embedded with rutile nanocrystals, *Adv. Funct. Mater.*, 2007, **17**, 2133–2138.

63 H. Tang, K. Prasad, R. Sanjinès, P. E. Schmid and F. Lévy, Electrical and optical properties of TiO₂ anatase thin films, *J. Appl. Phys.*, 1994, **75**, 2042–2047.

64 A. O. Govorov, H. Zhang, H. V. Demir and Y. K. Gun'ko, Photogeneration of hot plasmonic electrons with metal nanocrystals: Quantum description and potential applications, *Nano Today*, 2014, **9**, 85–101.

65 S. Naya, T. Kume, R. Akashi, M. Fujishima and H. Tada, Red−Light−Driven Water Splitting by Au(Core)−CdS(Shell) Half−Cut Nanoegg with Heteroepitaxial Junction, *J. Am. Chem. Soc.*, 2018, **140**, 1251–1254.

66 E. Thimsen, F. Le Formal, M. Grätzel and S. C. Warren, Influence of plasmonic Au nanoparticles on the photoactivity of Fe₂O₃ electrodes for water splitting, *Nano Lett.*, 2011, **11**, 35–43.

67 Q. Chen and Y. Tan, Enhanced plasmonic absorption of Pt cuboctahedra-WO₃ nanohybrids used as visible light photocatalysts for overall water splitting, *Nano Res.*, 2023, **16**, 5919–5928.

68 R. Kojima, S. Naya and H. Tada, Three-dimensional plasmonic photocatalyst consisting of faceted gold nanoparticles and radial titanium(IV) oxide heteromesocrystal, *J. Phys. Chem. C*, 2023, **127**, 3478–3485.